ACS APPLIED MATERIALS & INTERFACES

Research Article

www.acsami.org

Facile Fabrication of Single-Phase Multifunctional $BaGdF_5$ Nanospheres as Drug Carriers

Qi Zhao,[†,§] Zhen Lei,[‡,§] Sa Huang,[∥] Xueli Han,[∥] Baiqi Shao,[†,§] Wei Lü,[†] Yongchao Jia,[†,§] Wenzhen Lv,[†,§] Mengmeng Jiao,[†,§] Zhenxin Wang,*[,‡] and Hongpeng You*[,†]

[†]State Key Laboratory of Rare Earth Resource Utilization, Changchun Institute of Applied Chemistry, Chinese Academy of Sciences, Changchun 130022, People's Republic of China

[‡]State Key Laboratory of Electroanalytical Chemistry, Changchun Institute of Applied Chemistry, Chinese Academy of Sciences, Changchun 130022, People's Republic of China

[§]University of the Chinese Academy of Sciences, Beijing 100049, People's Republic of China

[∥]Department of Radiology, the Second Hospital of Jilin University, Changchun 130022, People's Republic of China

Supporting Information

ABSTRACT: Multifunctional $BaGdF_5$ nanospheres with mesoporous, luminescent, and magnetic properties have been successfully synthesized with the assistance of trisodium citrate by a hydrothermal method. The mesoporous structure is revealed by scanning electron microscope and transmission electron microscope images as well as N_2 adsorption−desorption isotherm. The as-synthesized $BaGdF_5$ nanospheres exhibit an intense broad bluish emission (centered at 450 nm) under the excitation of 390 nm, which might originate from the $CO_2^{\cdot -}$ radical-related defect produced by Cit^{3-} groups. It is also shown that these $BaGdF_5$ nanospheres brightened the T_1-weighted images, suggesting that they could act as T_1 contrast agents for magnetic resonance imaging. Using metformin hydrochloride as the model drug, the luminescent porous spheres show good drug storage/release capability. Furthermore, the emission intensity varies as a function of the cumulative drug release, making the drug-carrying system easily trackable and monitorable by detecting the luminescence intensity. Additionally, the paramagnetic property, originating from the unpaired electrons of Gd^{3+} ions, opens the possibility of directing the magnetic targeted carrier to the pathological site by magnetic field gradient.

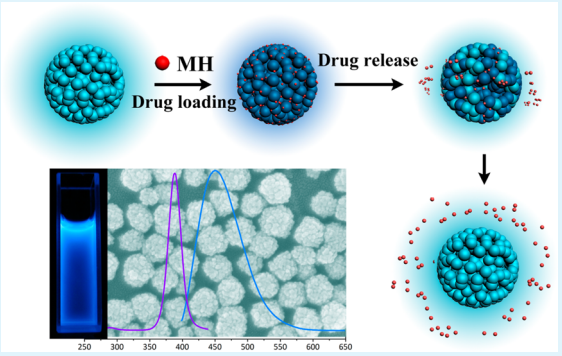

KEYWORDS: *$BaGdF_5$, multifunctional material, luminescence, porosity, magnetism, drug delivery*

INTRODUCTION

Recently, multifunctional nanosystems with integrated capabilities are at the forefront of scientific research because of their potential applications in many fields, including energy storage, medical diagnosis, cancer therapy, etc.[1−6] In particular, the nanomaterials combining luminescent, magnetic, and porous properties have attracted increasing attention due to the great promise as a smart drug carrier.[7−9] First, magnetic nanoparticles loaded with pharmaceuticals can be directed specifically to pathological sites by utilizing magnetic attraction.[10] Second, the integration of magnetic and luminescent properties yields the nanoprobe that can perform optical and magnetic resonance (MR) dual-modal imaging simultaneously for real-time visualization.[11] Third, the porous materials have been widely used as drug delivery hosts because of the large inner space and high surface area.[12] Usually, the multifunctionality is based on the structural integration of several nanospecies with different properties. The typical strategies include coating a shell layer on the core[13−16] or encapsulating active components into the host materials.[17−19] A significant challenge associated with the multifunctional conjugation is that one of the components not only retains its intrinsic properties but also should not interfere with the properties of other components.[20,21] However, it is complex and difficult to assemble two or more functional components through chemistry synthesis. Therefore, it is highly valuable to design and develop single-phase multifunctional nanoparticles without any other moieties for the simultaneous optical/MR imaging and targeted drug delivery.

As is known, Gd^{3+} ions have unpaired inner 4f electrons closely bound to the nucleus and shielded by the outer shell electrons $5s^25p^6$ from the crystal field.[22] The large magnetic moment and nanosecond time scale electronic relaxation time made them ideal paramagnetic relaxation agents. Thus, Gd^{3+}-based compounds are approved to be an excellent candidate as contrast agents for MR imaging and as carriers for magnetism-

Received: May 5, 2014
Accepted: June 30, 2014
Published: July 10, 2014

assisted drug delivery.[23−25] In biological applications, the luminescent materials, mainly including fluorescent dyes (FDs) and quantum dots (QDs), were extensively investigated for biolabeling, bioimaging, diagnostics, etc.[26−28] However, their disadvantages of photobleaching and quenching blinking for FDs and potential cytotoxicity in vivo for QDs as well as the complex functionalization strategies have limited their biomedical applications. In recent years, a class of self-activated luminescent materials has been synthesized, in which the luminescence was attributed to the defects or radical impurities.[29,30] The defect-related luminescent materials can be a good alternative for biomedical applications, considering the advantages of efficient emission, low cost, and nontoxicity. However, there was no report on combining the defect-related luminescence and the magnetism for drug delivery.

Herein, we fabricated $BaGdF_5$ porous nanospheres with the assistance of trisodium citrate, which show magnetic-optic bifunctional properties. The self-activated luminescence performance and the growth process of the spherical structure were discussed in detail. Additionally, the drug storage and release properties were also studied using metformin hydrochloride (MH) as the model drug.

EXPERIMENTAL SECTION

Chemicals and Materials. The rare-earth oxide Gd_2O_3 (99.99%) was supplied by Shanghai Yuelong Non-Ferrous Metals Co., Ltd. Metformin hydrochloride was purchased from Xi'an Yue Lai Medical Technology Co., Ltd. The other analytical chemicals (barium chloride, trisodium citrate, sodium fluoborate, and butylamine) were all supplied by Beijing Chemical Co. $GdCl_3$ stock solutions were prepared by dissolving the Gd_2O_3 in HCl solution under heating with vigorous stirring. The excess HCl was evaporated until the pH value of the solution was 4.

Preparation of Porous Nanospheres of $BaGdF_5$. In a typical procedure, 0.6 g of trisodium citrate was dissolved in 20 mL of deionized water to form a transparent solution. Then, 1 mL of $GdCl_3$ (1 mol·L^{-1}) and 1.5 mL of $BaCl_2$ (1 mol·L^{-1}) aqueous solution were added into the above solution. After vigorous stirring for 10 min, a 17 mL aqueous solution containing 0.16 g of $NaBF_4$ was introduced into the mixture. Subsequently, a certain amount of butylamine was added dropwise, adjusting the pH value to 10. After additional agitation for 15 min, the feedstock was transferred to a 50 mL Teflon-lined stainless autoclave and maintained at 180 °C for 4 h. The products were separated and collected by centrifugation and washed several times with ethanol and deionized water.

Cell Culture and Cytotoxicity Test. The Hela cell line was provided by the Shanghai cell bank of Chinese Academy of Science (Shanghai, China). Dulbecco's modified Eagle's medium (DMEM) and fetal bovine serum (FBS) was purchased from HyClone Co. (USA). Hela cells were seeded in 96-well plates at a density of 8000 cells per well and was cultured at 37 °C in 5% CO_2 for 24 h. Subsequently, the Hela cells were washed with fresh medium and incubated with $BaGdF_5$ nanoparticles at desired concentrations for another 24 h, respectively. Then, the Hela cells were washed with 100 μL of PBS (pH = 7.4) and incubated with 10 μL of 3-(4,5-dimethylthiazol-2-yl)-2,5-diphenyltetrazolium bromide (MTT) (5 mg·mL^{-1} in PBS) plus 100 μL of fresh medium at 37 °C with 5% CO_2 for 4 h. Finally, the medium containing MTT was removed, and the formazan crystals were dissolved by dimethyl sulfoxide (DMSO, 100 μL per well) and shaken for 5 min, respectively. The absorbance of each well was measured at 550 nm by a microplate reader (Power Wave XS2, BioTekCo., USA). Cells cultured without $BaGdF_5$ were used as a control sample. The relative cell viabilities (%) were determined as the ratio of the absorbance value to the control value.

In Vitro MR Imaging. The T_1-weighted MR images were obtained using a 1.5 T Philips MR Systems Achieva (Philips Medical Systems, Nederland B.V.). Dilutions of $BaGdF_5$ nanoparticles in PBS buffer solution (pH = 6.8) with expected concentrations (0, 0.1, 0.2, 0.4, 0.8, and 1 mM) were placed in a series of 4.0 mL Eppendorf tubes for T_1-weighted MR imaging.

Preparation of Drug Storage/Delivery Systems. The drug storage/release system was prepared following a literature method.[29,31] Typically, 0.17 g of $BaGdF_5$ sample was dispersed in 30 mL of MH aqueous solution (60 mg·mL^{-1}) in a sealed flask and soaked for 24 h at room temperature with slow stirring. The MH-loaded $BaGdF_5$ sample was collected by centrifugation and then dried at 60 °C in air for 24 h.

The in vitro delivery study was conducted by immersing 150 mg of $BaGdF_5$−MH in 150 mL of phosphate buffer solution (PBS, pH = 6.8) at a rotational speed of 100 rpm at (37 ± 0.5)°C. Samples (0.5 mL) were withdrawn at regular intervals and replaced with the same volume of release media. The withdrawn samples was then centrifuged at 6000 rpm over 4 min, and the supernatant was decanted. Then, the aliquots were diluted to a desired concentration (2−20 μg·mL^{-1}) by PBS and analyzed by UV−vis spectroscopy (Shimadzu UV-3600) at 231 nm using PBS as a reference. The concentration of MH was determined by the standard curve of MH in PBS, which is preprepared (see the Supporting Information). The dissolution test was performed in triplicate.

Characterization. X-ray diffraction (XRD) measurement was performed on a D8 Focus diffractometer (Bruker). Fourier transform infrared spectroscopy (FT-IR) spectra were measured using a PerkinElmer 580B infrared spectrophotometer with the potassium bromide pellet technique. The morphologies and size were determined by a field emission scanning electron microscope with energy-dispersive spectrometry (EDS) (S-4800, Hitachi, Japan). Transmission electron microscopy (TEM) was performed on a JEOL-2010 (Japan) microscope operating at 200 kV. Nitrogen adsorption/desorption analysis was performed on a Micromeritics (NOVA 4200e) analyzer. Thermogravimetric analysis (TG) was measureed on a thermal analysis instrument (SDT2960, DE, New Castle) in an air flow of 100 mL min^{-1} at 10 °C min^{-1} from room temperature to 1000 °C. Photoluminescence spectra were recorded on a Hitachi F-7000 spectrophotometer using a 150 W xenon lamp as the excitation source. The luminescence decay curves were measured at an FLS-920 combined fluorescence lifetime and steady-state spectrometer (Edinburgh Instruments, UK). The field-dependent magnetization curve was recorded using Quantum Design-MPMS-XL7 magnetometer. All the measurements were performed at room temperature.

RESULTS AND DISCUSSION

Phase Structure, Morphology, and Formation Process of the $BaGdF_5$ Crystals. As shown in Figure 1a, all the XRD peaks of the representative sample can be readily indexed as cubic $BaGdF_5$ (JCPDS No. 24-0098). The EDS spectrum in Figure 1b exhibits the presence of barium (Ba), gadolinium (Gd), fluorine (F), and carbon (C) in the as-prepared $BaGdF_5$ sample. The detected carbon impurity might result from the trisodium citrate, which was employed as organic chelating ligand in the hydrothermal process.

SEM and TEM techniques were employed to characterize the morphologies and structures of the samples. A panoramic SEM image (Figure 2a) demonstrates that the sample consists of well-dispersed nanospheres with a narrow diameter distribution in the range of 65−119 nm (Figure 2d). Further close observation under higher magnification reveals that the sphere-like structures are composed of many smaller nanoparticles with a size of about 5−12 nm (Figure 2b). Numerous subunits aggregate together tightly to form the spherical structure. The TEM images (Figure 2c) further confirm the stacking of the building blocks and the porous structure of the $BaGdF_5$ spheres considering the different electron penetrability.

The porous nature of the $BaGdF_5$ spheres was investigated through nitrogen sorption measurements. Figure 3 shows the N_2 adsorption/desorption isotherms and corresponding pore

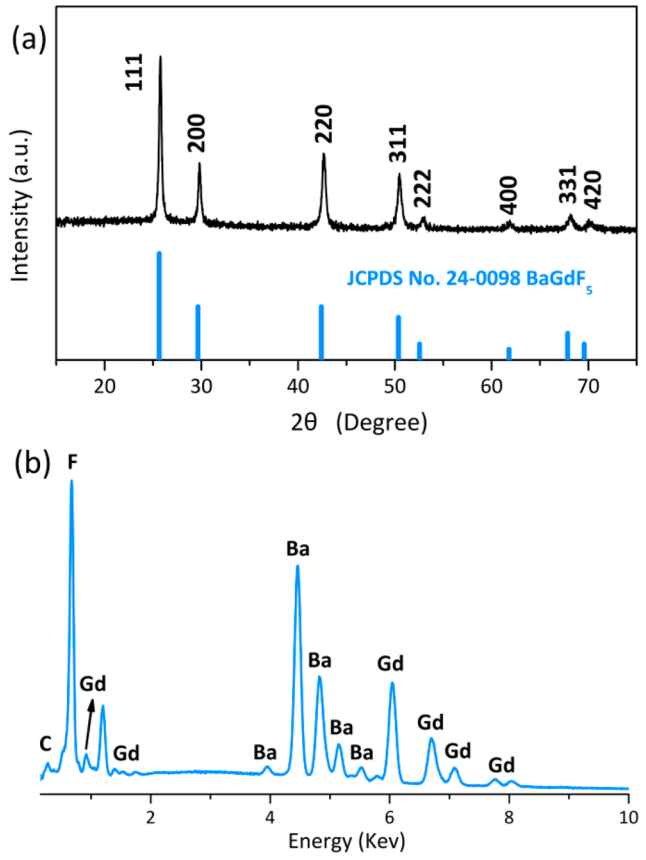

Figure 1. (a) XRD pattern and (b) EDS spectrum of the as-prepared $BaGdF_5$ sample.

size distributions of the $BaGdF_5$ nanoparticles. The sample shows IV-type isotherms and H1 hysteresis loops, which are characteristic of typical mesoporous materials. The Brunauer–Emmett–Teller (BET) surface area is about 131.12 m^2/g, and the pore volume is 0.30 cm^3/g, calculated from N_2 isotherms. The pore size distribution plot, obtained by the Barrett–Joyner–Halenda (BJH) method, shows a striking peak at 2.47 nm (inset in Figure 3). The mesopores are attributed to the interstitial spaces between the subunits of the $BaGdF_5$ spheres, which coincides with the SEM and TEM observations. These results confirm the existence of mesoporous structures in $BaGdF_5$ nanospheres and open the possibility for future application in drug delivery systems.

As is known, citrate can coordinate with metal cations and adsorb on the crystal surface, which significantly alters crystal growth behavior in the synthesis of nanomaterials.[32,33] The FT-IR spectroscopy for the typical $BaGdF_5$ sample (Figure 4a) show the bands at 1578 and 1407 cm^{-1} due to the asymmetric and symmetric of the carboxylic group ($-COO^-$), which confirms the adsorption of Cit^{3-} on the $BaGdF_5$ crystals. The absorption band at 3427 cm^{-1} is ascribed to the O–H stretching vibration of absorbed H_2O. To investigate the effect of trisodium citrate (TSC) on the growth process of the $BaGdF_5$ sample, the contrast experiments were conducted varying the TSC amounts. As is shown in Figures S1a and S2a (Supporting Information), microrods of hexagonal $NaGdF_4$, rather than $BaGdF_5$ nanospheres, were obtained without TSC. In the presence of TSC (0.2–1.5 g), the products adopted the same pure cubic $BaGdF_5$ phase (Figure S2b–f, Supporting Information). When the addition of TSC was 0.2 g, the products consisted of irregularly shaped nanoparticles (Figure S1b, Supporting Information). Spherical aggregates with broad size distributions came into being after increasing the TSC to 0.4 g, and the components were connected loosely (Figure S1c, Supporting Information). When the added TSC was more than 0.6 g, uniform nanospheres were obtained, which were assembled by small particles (Figure S1d–f, Supporting Information). Moreover, the size of the sphere-like structure decreased as the TSC amount increased. On the basis of experimental results, the functions of the TSC can be interpreted as follows. In the TSC-riched solution, the citrate groups were reacted with Gd^{3+} and Ba^{2+} ions to form the metal–Cit^{3-} complex. During the hydrothermal process, the F^-

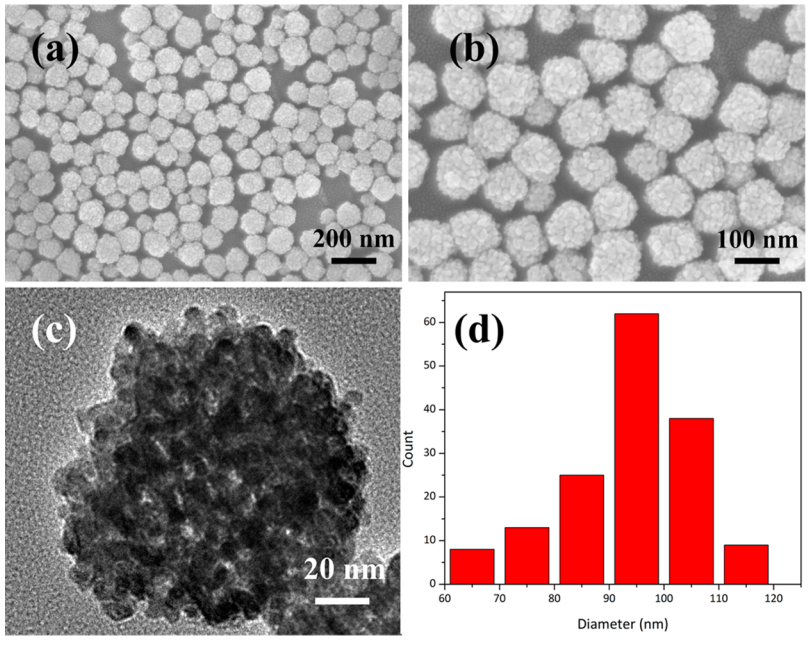

Figure 2. (a, b) SEM images, (c) TEM image, and (d) size distribution of the as-prepared $BaGdF_5$ sample.

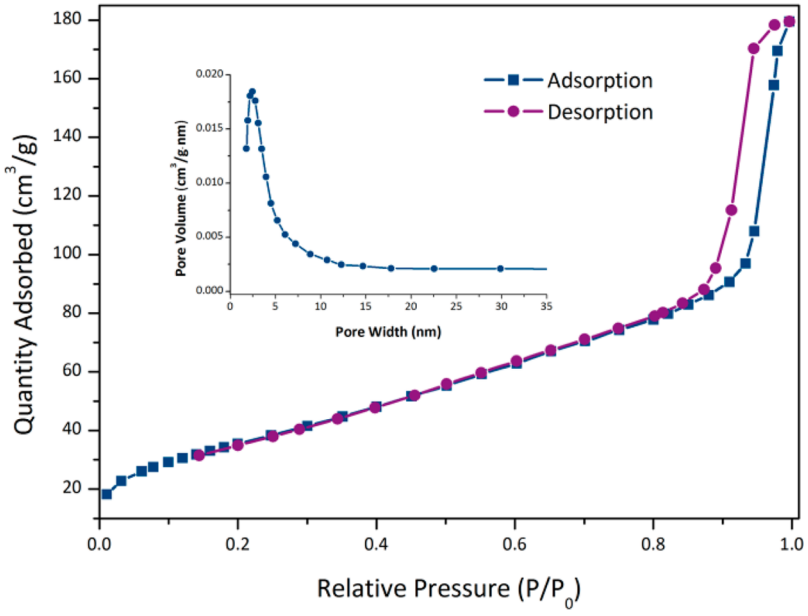

Figure 3. N_2 adsorption/desorption isotherms of the $BaGdF_5$ nanospheres. Inset: the pore size distribution curve calculated from the adsorption data.

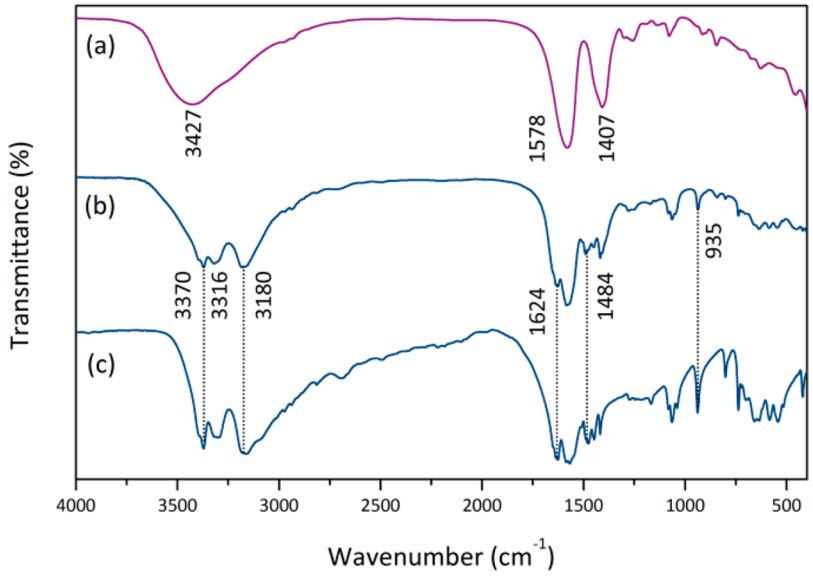

Figure 4. FT-IR spectra for (a) $BaGdF_5$ sample, (b) MH-loaded $BaGdF_5$, and (c) pure MH.

ions attacked the complex, and a crystal nucleation process occurred to generate $BaGdF_5$ nuclei. As the reaction continued, the primary particles further assembled to form the final products driven by the adsorbed citrate groups (electrostatic, hydrogen, coordination bonds, etc.). The assumption was confirmed by the fact that the nanoparticle failed to assemble together when the TSC was deficient (Figure S1b, Supporting Information). Besides, the citrate in the solution would cap on the as-formed nanospheres to prevent excessive growth. However, the crystal nucleation and mass transfer would be inhibited to some extent if the added TSC was overmuch.[34] Thereby, the smaller aggregates were yielded which consisted of less subunit. The formation process of the mesoporous $BaGdF_5$ is schematically shown in Scheme 1. Accordingly, it can be concluded that the TSC played an important role in the formation of the monodisperse porous nanospheres of $BaGdF_5$.

Luminescence Mechanism. The excitation (purple line) and emission (blue line) spectra of the as-synthesized $BaGdF_5$ is shown Figure 5a. The $BaGdF_5$ sample exhibits a strong and broad emission band ranging from 400 to 550 nm centered at 450 nm, and the excitation spectrum is composed of a broadband peaking at 390 nm. Figure 5b shows the fluorescent decay curve for the $BaGdF_5$ sample. The decay curve can be fitted to a single exponential function as $I = I_0\exp(-t/\tau)$, from which the decay lifetime τ is calculated to be 7.05 ns.

Because no activator ions (rare-earth or transition-metal ions) were doped, and Ba^{2+}, Gd^{3+}, or F^- ions show no emission in the band from 400 to 550 nm, the observed blue luminescence was assumed to originate from the impurities or defects, which was characterized by the short decay time (7.05 ns).[35] As is known, the Cit^{3-} groups can adsorb on the crystal planes owing to their strong chelating ability.[29] Under

Scheme 1. Schematic Illustration for the Formation Process of Luminescence Porous $BaGdF_5$ Nanopheres and Subsequent Drug Loading and Release

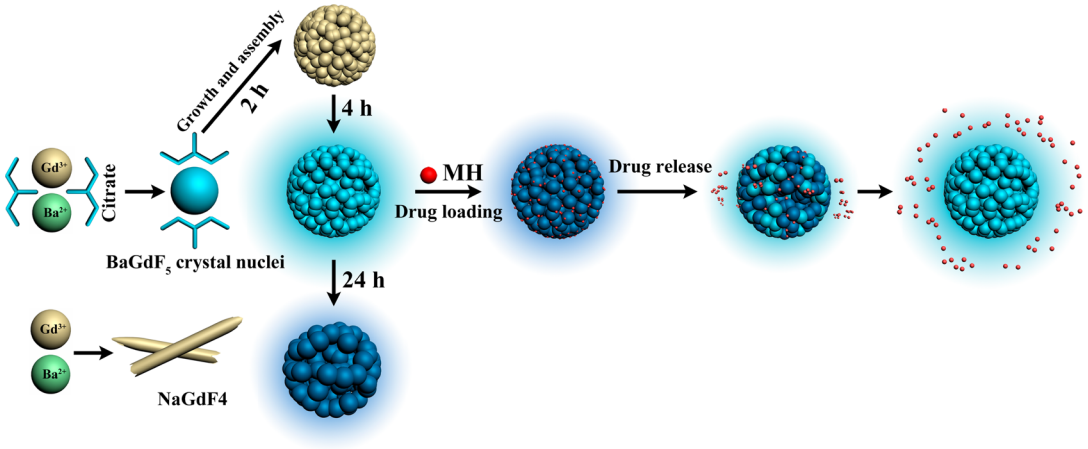

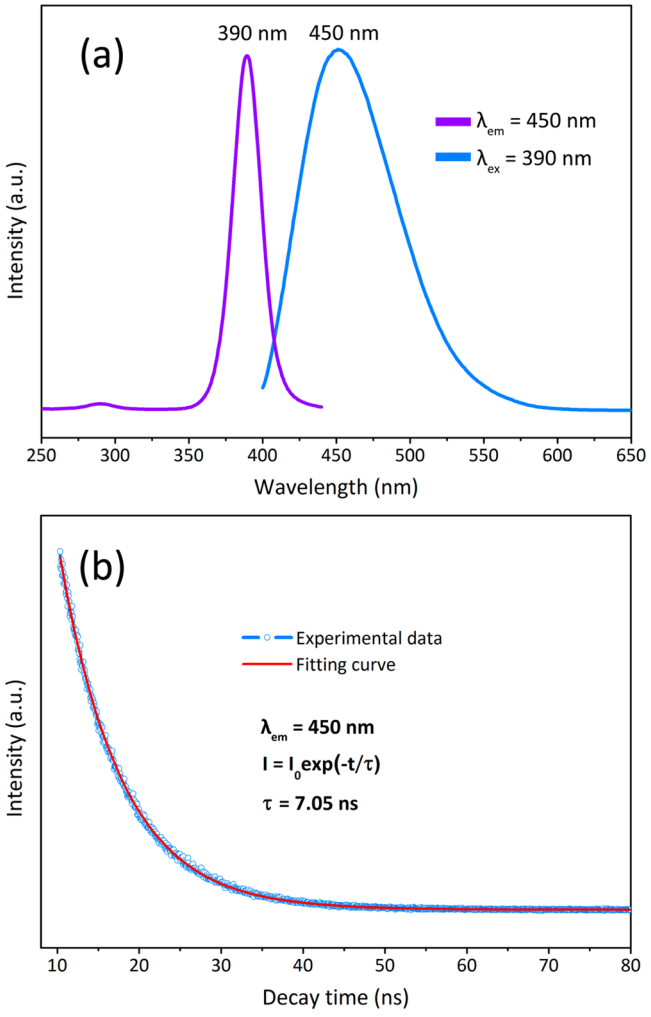

Figure 5. (a) Excitation (purple line) and emission (blue line) spectra and (b) the decay curve of the as-prepared $BaGdF_5$ sample.

the high pressure and temperature in the hydrothermal process, the bond cleavages of the R−C−COO^- group occurred to produce R−C· and $CO_2{\cdot}^-$.[29,30] Some newly formed $CO_2{\cdot}^-$ radicals were trapped by the $BaGdF_5$ lattice to form radical-related defect center. These carbon dioxide radical anions may become optically active centers of self-activated luminescence through a strong electron−photon coupling.[29] Therefore, the trisodium citrate (TSC) might be responsible for the formation of defects in the host lattice.

To verify the assumptions, the TSC-dependent luminescence intensity variations were investigated. As is shown in Figure 6a, the product shows no luminescence under 390 nm excitation when TSC was absent. Upon increasing the TSC to 0.2 g, the as-synthesized $BaGdF_5$ showed weak blue luminescence centered at 450 nm. The emission was enhanced significantly when the TSC amount increased to 0.4 g. The $BaGdF_5$ nanospheres prepared with TSC of 0.6 g shows the strongest blue emission, and the sample synthesized with 0.8 g of TSC gives the second strongest emission intensity. With further increasing the TSC addition to 1.5 g, the emission intensity decreased more. The inset of Figure 6a shows the dependence of the integral luminescence intensity of the $BaGdF_5$ nanospheres on the TSC amount. These results allow us to conclude that the TSC endows the synthesized $BaGdF_5$ nanospheres with the defect-related luminescent features. When more TSC was added in the reaction system, more luminescent centers would be created, thereby, the luminescence intensity was increased. However, overmuch TSC could decrease the emission intensity because of the quenching effect of the luminescent centers.

Beside from the Cit^{3-} amount, the reaction time also has an important effect on the defect-related luminescence. The $BaGdF_5$ sample obtained after reacting for 2 h gives nearly no emission, although the porous spheres have been yielded (Figures 6b, S3, and S4, Supporting Information). It is supposed that the $CO_2{\cdot}^-$ radicals failed to form in such a short time. The luminescent intensity increased dramatically when the reaction time was prolonged to 4 h. Unexpectedly, the luminescence was weakened after increasing the hydrothermal time to 6 h. Upon further prolonging the hydrothermal treatment to 12 and 24 h, the luminescence emission became very weak, which is different from the precious report.[36] The SEM images of the intermediates (Figure S3, Supporting Information) show that the morphologies revealed no significant differences except that the building blocks grew larger as the reaction time increased. This is because the Ostwald ripening was going on during the hydrothermal process, i.e., small crystals dissolve and redeposit onto larger crystals.[37] In this crystallites relocation process, the interstitial defects would migrate out from the $BaGdF_5$ lattice, which is the

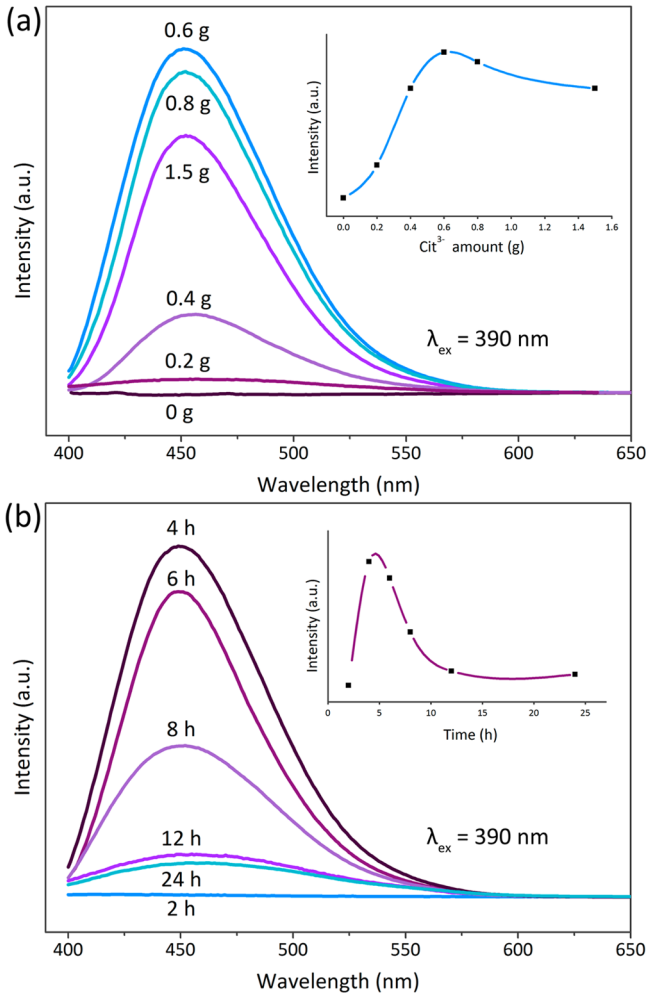

Figure 6. (a) Photoluminescence emission spectra of $BaGdF_5$ samples prepared at different TSC amounts. The inset shows the dependence of the luminescence intensity of the $BaGdF_5$ nanospheres on the TSC amount. (b) Photoluminescence emission spectra of $BaGdF_5$ samples obtained after different reaction time. The inset shows the luminescence intensity as a function of hydrothermal time.

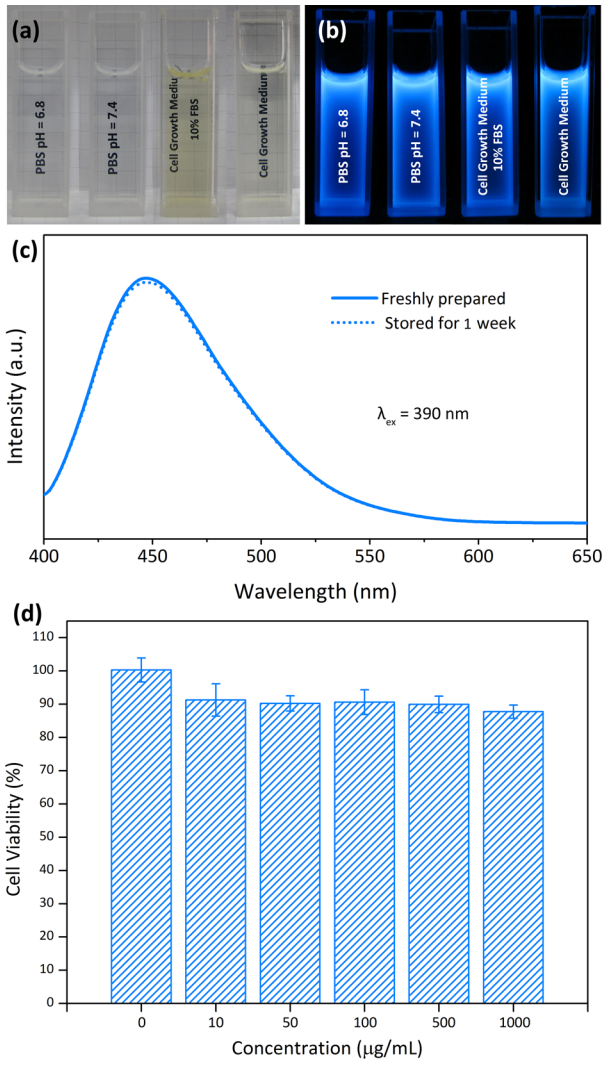

Figure 7. Photographs of (a) $BaGdF_5$ nanoparticles dispersed in phosphate buffer solution (pH = 6.8, 7.4), serum supplemented cell growth medium (DMEM), and serum-free cell culture media (DMEM) and (b) respective luminescence under 365 nm excitation. (c) Spectra of freshly prepared $BaGdF_5$ dispersion in PBS (pH = 6.8) (solid line) and sample after being stored for 1 week (dot line). (d) In vitro cell viability of Hela cells incubated with $BaGdF_5$ nanoparticles at different concentrations for 24 h at 37 °C (n = 5).

so-called self-purification process.[33] As we have discussed above, the luminescence resulted from the $CO_2{\cdot}^-$ radicals. Therefore, it is speculated that the emission intensity was decreased with extension of the reaction time because of the outward migration of the radical-related defects. The effect of citrate and reaction time are summarized in Scheme 1.

Stability and Cytotoxicity. The stability of nanoparticles in a biological growth medium is of paramount importance for biomedical applications. In our case, the as-synthesized $BaGdF_5$ (2 mg·mL^{-1}) was dispersed well in phosphate buffer solution (pH = 6.8, 7.4), serum supplemented cell growth medium (DMEM), and serum-free cell culture media (DMEM) and no observable aggregation of nanoparticles was found after 1 week (Figure 7a,b). Because additional surface modification was not involved in the synthesis procedure, it is speculated that the citrate served as a capping agent to stabilize the nanoparticles from aggregation. The FT-IR spectroscopy (Figure 4a) and TG curve (Figure 9b) also confirmed the existence of citrate adsorbed on the $BaGdF_5$ crystals. In addition, the samples show slight changes of luminescence intensity after being stored under chamber conditions for 1 week (Figures 7c and S5, Supporting Information). These results indicate that the as-prepared $BaGdF_5$ nanospheres have good colloidal and optical stabilities.

To evaluate the biocompatibility of the materials for their potential biological applications, a MTT assay with HeLa cells was performed on the $BaGdF_5$ nanoparticles. Figure 7d shows that the cell viability was more than 90% with different concentrations ranging from 10 to 500 μg·mL^{-1}. Upon further increasing the concentration of $BaGdF_5$ nanospheres to 1000 μg·mL^{-1}, cell viability is still greater than 88%, suggesting the cytotoxicity of $BaGdF_5$ nanoparticles is low. Therefore, it can be safely concluded that the porous spheres show satisfactory biocompatibility of in all dosages.

Paramagnetic Properties and MR Imaging. Figure 8a shows the field-dependent magnetization curve of $BaGdF_5$ at 300 and 3 K. The nanospheres are paramagnetic at 300 K and the magnetic mass susceptibility of the $BaGdF_5$ nanoparticles was determined to be 9.27×10^{-5} emu·Oe^{-1}·g^{-1}. The magnetization is 1.93 and 4.66 emu·g^{-1} at 20 and 50 kOe,

dx.doi.org/10.1021/am502718b | ACS Appl. Mater. Interfaces 2014, 6, 12761−12770

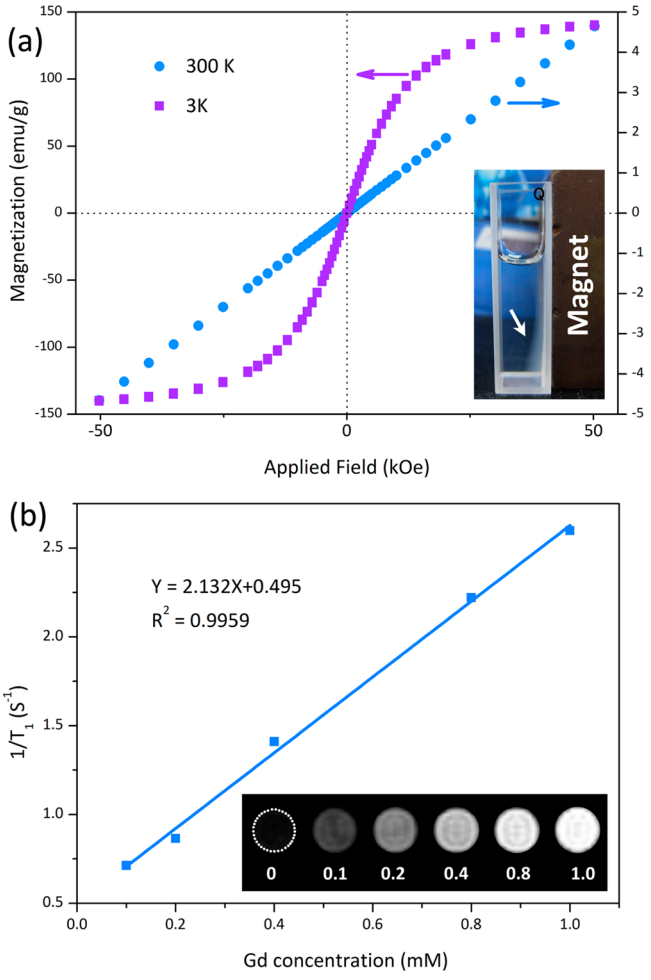

Figure 8. (a) Magnetization curves of the $BaGdF_5$ nanospheres at 300 and 3 K. Inset: photo of $BaGdF_5$ nanoparticles colloidal solution with a neighboring magnet. (b) Relaxation rate ($1/T_1$) versus various molar concentrations of $BaGdF_5$ nanoparticles dispersions at room temperature using a 1.5 T MRI scanner. Inset: T_1-weighted images of various molar concentrationsof $BaGdF_5$.

respectively, which is similar to the reported value.[38−43] Besides, at 3 K, the nanospheres are superparamagnetic with saturation magnetization values of 140 emu·g^{-1}. As shown in the inset of Figure 8a, the nanoparticles were attracted to one side of the cuvette by a magnet at room temperature. Therefore, the as-synthesized $BaGdF_5$ porous spheres might find potential application as a smart drug carrier in targeted drug delivery with assistance of an external magnetic field.

To further demonstrate the $BaGdF_5$ spheres as a potential MRI contrast agent, T_1 relaxatiom time was measured in PBS buffer (pH = 6.8) dispersions with different Gd^{3+} concentrations. The longitudinal relaxivity (r_1) was calculated to be 2.132 $s^{-1}(mM)^{-1}$ from the slope of concentration-dependent relaxation rate ($1/T_1$) (Figure 8b). In a proof-of-concept application as MR imaging contrast agents (inset of Figure 8b), the T_1-weighted MRI signal intensity was clearly enhanced as the concentration of Gd^{3+} increased. These results suggest that the $BaGdF_5$ nanoparticles may serve as an efficient T_1-weighted MRI contrast agents, which can offer imaging modality to monitor the drug delivery by MRI.

Drug Adsorption and Release Properties. The drug storage/release properties of the $BaGdF_5$ porous spheres were investigated, taking metformin hydrochloride (MH) as a model drug. As is shown in the FT-IR spectroscopy measurement of the MH-loaded $BaGdF_5$ (Figure 4b), the absorption bands at 3370, 3316, and 3180 cm^{-1} were assigned to the asymmetric and symmetric stretching vibrations of N—H arising from the introduced MH (Figure 4c). Furthermore, the bands at 1624, 1484, and 935 cm^{-1} were attributed to C═N stretching vibrations, CH_3 asymmetric deformation, and N—H wagging, respectively, in MH molecular. This confirms the successful incorporation of MH into the $BaGdF_5$ nanospheres. The loading amount of MH in $BaGdF_5$ nanospheres was determined as 25.1 wt % according to the absorbance variation of the MH aqueous solution before and after interaction with $BaGdF_5$ (Figure 9a), which is basically consistent with the

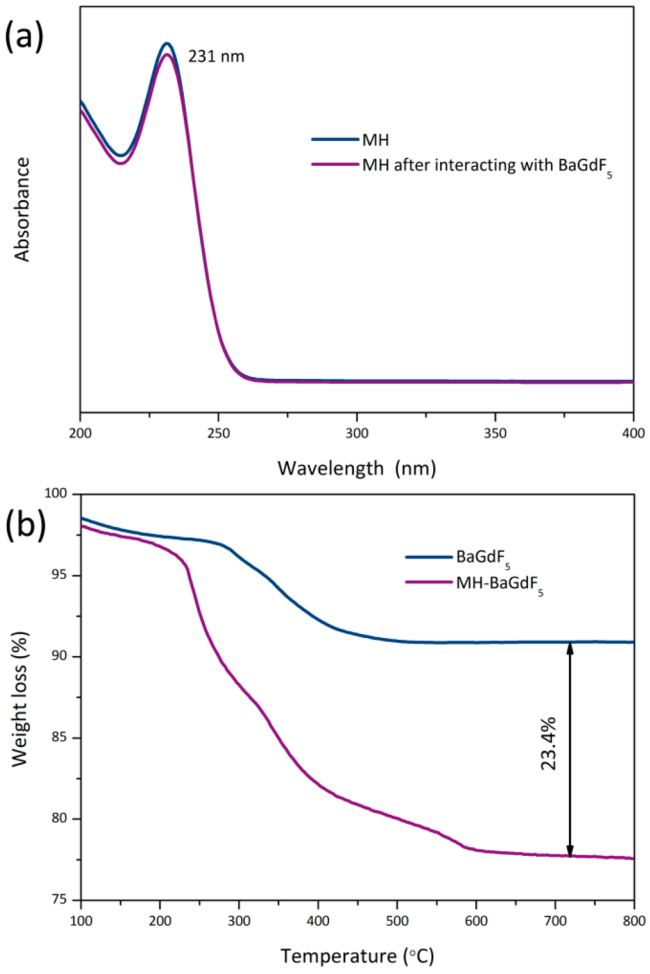

Figure 9. (a) UV absorbance spectra of the MH aqueous solution before and after the interaction with $BaGdF_5$. (b) TG curves of the $BaGdF_5$ and $BaGdF_5$−MH samples.

result (23.4 wt %) calculated by the thermogravimetric (TG) analysis (Figure 9b). It should be noted that the weight loss occurred at about 300 °C in $BaGdF_5$ sample was ascribed to the decomposition of trisodium citrate, which capped on the crystal surface. The high loading amount was ascribed to the porous structures of $BaGdF_5$ nanospheres, which can entrap the drug molecular by an impregnation process. During the release process, the stored MH would be liberated from the porous nanospheres dominated by a diffusion-controlled mode. Figure 10a shows the cumulative drug release profiles in $BaGdF_5$−MH as a function of release time. The system experienced a burst

dx.doi.org/10.1021/am502718b | ACS Appl. Mater. Interfaces 2014, 6, 12761−12770

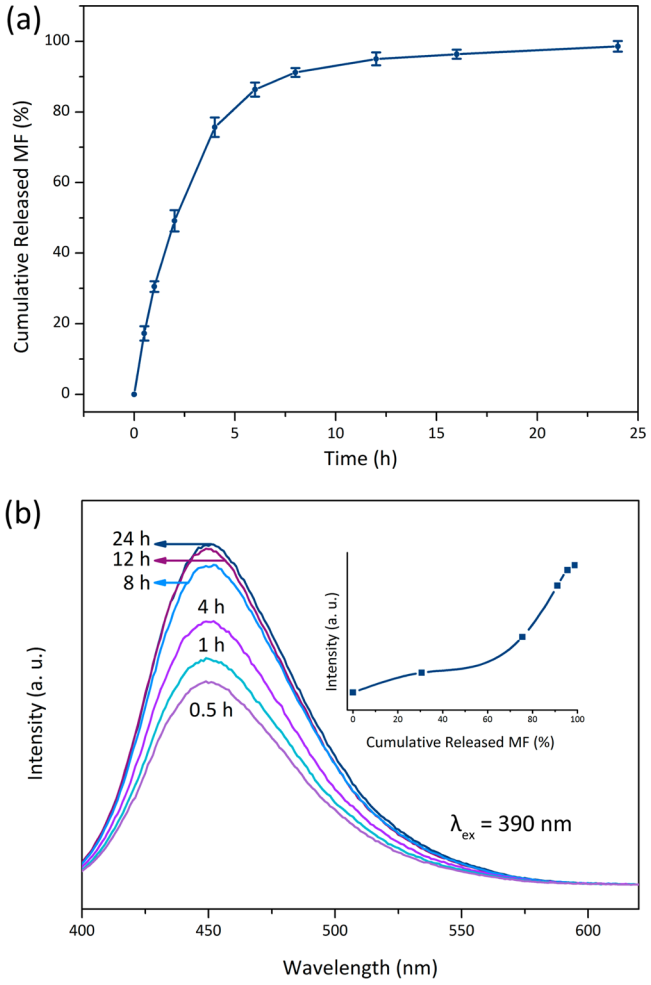

Figure 10. (a) Cumulative MH release from $BaGdF_5$–MH system as a function of release time in PBS. Values are presented as the mean ± standard deviation of three experiments (n = 3). (b) Photoluminescence emission spectra of $BaGdF_5$–MH system at different release times. Inset in panel b shows the dependence of the luminescence intensity of the $BaGdF_5$–MH on the cumulative released MH.

release of 49.2 ± 3.0% within 2 h and 86.4 ± 2.1% within 6 h, followed by a relatively slow release and complete release after 12 h. The initial rapid release was resulted from the MH molecules weak adsorption on the outside surface of $BaGdF_5$ nanospheres, and the slow release of the remaining of MH can be ascribed to the adsorption on the internal surface of the mesoporous sphere.

Moreover, the luminescence intensity was affected by the drug loading. Figure 10b shows the emission spectra of the $BaGdF_5$–MH system at different release times. The profile and peak position of the emission spectra of $BaGdF_5$–MH samples did not show significant changes, but the emission intensity increases with prolonged drug release time. Considering that the cumulative released MH is basically proportional to the release time, it is assumed that the defect-related luminescence was weakened by the adsorbed MH molecules and would recover after the drug released from the $BaGdF_5$ porous spheres (inset of Figure 10b). This phenomenon can be a result of the quenching effect of defect-related luminescence by the loaded MH molecules, which have many organic groups with high phonon energies. As the release time increases, more MH molecules are released from the $BaGdF_5$–MH system and the quenching centers decrease, leading to the increase of luminescence intensity. This characteristic makes the drug delivery system easily identifiable, trackable, and monitorable by detecting the luminescence intensity. The loading and release of MH is schematically shown in Scheme 1.

CONCLUSIONS

In summary, single-phase multifunctional nanospheres of $BaGdF_5$ have been synthesized via a facile hydrothermal route. The SEM and TEM images reveal that the uniform nanospheres are actually aggregates of a large amount of smaller particles. The N_2 adsorption/desorption isotherms confirm the existence of mesoporous structures in the $BaGdF_5$ spheres. Under the excitation of 390 nm, the as-obtained nanospheres show strong blue (450 nm) emission in the absence of activator ions. The $CO_2^{\cdot -}$ radical-related defect produced by Cit^{3-} groups is responsible for the self-activated luminescence. The amount of the trisodium citrate in the initial solution and the hydrothermal treatment time has an important effect on the luminescent intensity. Moreover, the trisodium citrate also serves as a morphology-controlling agent in the formation of the spherical structure. Additionally, paramagnetic properties of the nanospheres were also observed, which resulted from the unpaired electrons of Gd^{3+} ions. The relaxivity measurements indicated that the $BaGdF_5$ nanospheres could serve as contrast agents for magneticre sonance (MR) imaging. Furthermore, $BaGdF_5$ nanoparticles show good drug storage/release capabilities. Notably, the luminescence intensity increases as the stored MH is liberated, thus enabling the drug release to be easily tracked. Therefore, the $BaGdF_5$ nanospheres are expected to be a promising nanoplatform for optical/MR imaging and targeted drug delivery on the basis of the magnetic-optic bifunctional properties and the porous nature.

ASSOCIATED CONTENT

Supporting Information

Experimental details for the preparation of standard calibration curve of MH in PBS and determination of the loading amount of MH in $BaGdF_5$ nanospheres, SEM images of samples prepared at different TSC amounts, XRD patterns of samples prepared at different TSC amounts, SEM images of $BaGdF_5$ samples obtained after reacting for different times, XRD patterns of $BaGdF_5$ samples obtained after reacting for different times, and spectra of freshly prepared $BaGdF_5$ nanoparticles. This material is available free of charge via the Internet at http://pubs.acs.org.

AUTHOR INFORMATION

Corresponding Authors

*H. You. Email: hpyou@ciac.ac.cn. Phone: +86-431-85262798. Fax: +86-431-85698041.

*Z. Wang. Email: wangzx@ciac.ac.cn. Phone: +86-431-85262243. Fax: +86-431-85262243.

Notes

The authors declare no competing financial interest.

ACKNOWLEDGMENTS

This work is financially supported by the National Natural Science Foundation of China (Grant Nos. 21271167 and 11304309) and the Fund for Creative Research Groups (Grant

No. 21221061), and the National Basic Research Program of China (973 Program, Grant No. 2014CB6438003).

REFERENCES

(1) Cheng, Z.; Al Zaki, A.; Hui, J. Z.; Muzykantov, V. R.; Tsourkas, A. Multifunctional Nanoparticles: Cost Versus Benefit of Adding Targeting and Imaging Capabilities. *Science* **2012**, *338*, 903−910.

(2) Rolison, D. R.; Long, J. W.; Lytle, J. C.; Fischer, A. E.; Rhodes, C. P.; McEvoy, T. M.; Bourg, M. E.; Lubers, A. M. Multifunctional 3D Nanoarchitectures for Energy Storage and Conversion. *Chem. Soc. Rev.* **2009**, *38*, 226−252.

(3) Shi, D.; Bedford, N. M.; Cho, H.-S. Engineered Multifunctional Nanocarriers for Cancer Diagnosis and Therapeutics. *Small* **2011**, *7*, 2549−2567.

(4) Lee, J. E.; Lee, N.; Kim, T.; Kim, J.; Hyeon, T. Multifunctional Mesoporous Silica Nanocomposite Nanoparticles for Theranostic Applications. *Acc. Chem. Res.* **2011**, *44*, 893−902.

(5) Naccache, R.; Chevallier, P.; Lagueux, J.; Gossuin, Y.; Laurent, S.; Vander Elst, L.; Chilian, C.; Capobianco, J. A.; Fortin, M.-A. High Relaxivities and Strong Vascular Signal Enhancement for $NaGdF_4$ Nanoparticles Designed for Dual MR/Optical Imaging. *Adv. Healthcare Mater.* **2013**, *2*, 1478−1488.

(6) Singh, R. K.; Patel, K. D.; Kim, J.-J.; Kim, T.-H.; Kim, J.-H.; Shin, U. S.; Lee, E.-J.; Knowles, J. C.; Kim, H.-W. Multifunctional Hybrid Nanocarrier: Magnetic CNTs Ensheathed with Mesoporous Silica for Drug Delivery and Imaging System. *ACS Appl. Mater. Interfaces* **2014**, *6*, 2201−2208.

(7) Veiseh, O.; Gunn, J. W.; Zhang, M. Design and Fabrication of Magnetic Nanoparticles for Targeted Drug Delivery and Imaging. *Adv. Drug Delivery Rev.* **2010**, *62*, 284−304.

(8) Pansare, V. J.; Hejazi, S.; Faenza, W. J.; Prud'homme, R. K. Review of Long-Wavelength Optical and NIR Imaging Materials: Contrast Agents, Fluorophores, and Multifunctional Nano Carriers. *Chem. Mater.* **2012**, *24*, 812−827.

(9) Zhang, F.; Braun, G. B.; Pallaoro, A.; Zhang, Y.; Shi, Y.; Cui, D.; Moskovits, M.; Zhao, D.; Stucky, G. D. Mesoporous Multifunctional Upconversion Luminescent and Magnetic "Nanorattle" Materials for Targeted Chemotherapy. *Nano Lett.* **2011**, *12*, 61−67.

(10) Todd, T.; Zhen, Z.; Tang, W.; Chen, H.; Wang, G.; Chuang, Y.-J.; Deaton, K.; Pan, Z.; Xie, J. Iron Oxide Nanoparticle Encapsulated Diatoms for Magnetic Delivery of Small Molecules to Tumors. *Nanoscale* **2014**, *6*, 2073−2076.

(11) Tian, G.; Gu, Z.; Liu, X.; Zhou, L.; Yin, W.; Yan, L.; Jin, S.; Ren, W.; Xing, G.; Li, S.; Zhao, Y. Facile Fabrication of Rare-Earth-Doped Gd_2O_3 Hollow Spheres with Upconversion Luminescence, Magnetic Resonance, and Drug Delivery Properties. *J. Phys. Chem. C* **2011**, *115*, 23790−23796.

(12) Wang, X.; Chen, D.; Cao, L.; Li, Y.; Boyd, B. J.; Caruso, R. A. Mesoporous Titanium Zirconium Oxide Nanospheres with Potential for Drug Delivery Applications. *ACS Appl. Mater. Interfaces* **2013**, *5*, 10926−10932.

(13) Liu, R.; Guo, Y.; Odusote, G.; Qu, F.; Priestley, R. D. Core−Shell Fe_3O_4 Polydopamine Nanoparticles Serve Multipurpose as Drug Carrier, Catalyst Support and Carbon Adsorbent. *ACS Appl. Mater. Interfaces* **2013**, *5*, 9167−9171.

(14) Ma, D.; Guan, J.; Dénommée, S.; Enright, G.; Veres, T.; Simard, B. Multifunctional Nano-Architecture for Biomedical Applications. *Chem. Mater.* **2006**, *18*, 1920−1927.

(15) Ma, Q.; Wang, J.; Dong, X.; Yu, W.; Liu, G.; Xu, J. Electrospinning Preparation and Properties of Magnetic-Photoluminescent Bifunctional Coaxial Nanofibers. *J. Mater. Chem.* **2012**, *22*, 14438−14442.

(16) Lu, B.-Q.; Zhu, Y.-J.; Ao, H.-Y.; Qi, C.; Chen, F. Synthesis and Characterization of Magnetic Iron Oxide/Calcium Silicate Mesoporous Nanocomposites as a Promising Vehicle for Drug Delivery. *ACS Appl. Mater. Interfaces* **2012**, *4*, 6969−6974.

(17) Peng, E.; Choo, E. S. G.; Tan, C. S. H.; Tang, X.; Sheng, Y.; Xue, J. Multifunctional PEGylated Nanoclusters for Biomedical Applications. *Nanoscale* **2013**, *5*, 5994−6005.

(18) Chen, Y.; Guo, F.; Qiu, Y.; Hu, H.; Kulaots, I.; Walsh, E.; Hurt, R. H. Encapsulation of Particle Ensembles in Graphene Nanosacks as a New Route to Multifunctional Materials. *ACS Nano* **2013**, *7*, 3744−3753.

(19) Liu, F.; He, X.; Liu, L.; You, H.; Zhang, H.; Wang, Z. Conjugation of $NaGdF_4$ Upconverting Nanoparticles on Silica Nanospheres as Contrast Agents for Multi-Modality Imaging. *Biomaterials* **2013**, *34*, 5218−5225.

(20) Ma, Q. L.; Yu, W. S.; Dong, X. T.; Wang, J. X.; Liu, G. X. Janus Nanobelts: Fabrication, Structure and Enhanced Magnetic-Fluorescent Bifunctional Performance. *Nanoscale* **2014**, *6*, 2945−2952.

(21) Shi, D. Integrated Multifunctional Nanosystems for Medical Diagnosis and Treatment. *Adv. Funct. Mater.* **2009**, *19*, 3356−3373.

(22) Wong, H.-T.; Chan, H. L. W.; Hao, J. H. Magnetic and Luminescent Properties of Multifunctional GdF_3:Eu^{3+} Nanoparticles. *Appl. Phys. Lett.* **2009**, *95*, 022512.

(23) Li, Y.-Y.; Yan, B.; Li, Q.-P. Bifunctional Heterometallic Ln^{3+}-Gd^{3+} (Ln = Eu, Tb) Hybrid Silica Microspheres: Luminescence and MRI Contrast Agent Property. *Dalton Trans.* **2013**, *42*, 1678−1686.

(24) Sun, C.; Lee, J. S.; Zhang, M. Magnetic Nanoparticles in MR Imaging and Drug Delivery. *Adv. Drug Delivery Rev.* **2008**, *60*, 1252−1265.

(25) Johnson, N. J. J.; Oakden, W.; Stanisz, G. J.; Scott Prosser, R.; van Veggel, F. C. J. M. Size-Tunable, Ultrasmall $NaGdF_4$ Nanoparticles: Insights into Their T_1 MRI Contrast Enhancement. *Chem. Mater.* **2011**, *23*, 3714−3722.

(26) Resch-Genger, U.; Grabolle, M.; Cavaliere-Jaricot, S.; Nitschke, R.; Nann, T. Quantum Dots Versus Organic Dyes as Fluorescent Labels. *Nat. Methods* **2008**, *5*, 763−775.

(27) Michalet, X.; Pinaud, F. F.; Bentolila, L. A.; Tsay, J. M.; Doose, S.; Li, J. J.; Sundaresan, G.; Wu, A. M.; Gambhir, S. S.; Weiss, S. Quantum Dots for Live Cells, in Vivo Imaging, and Diagnostics. *Science* **2005**, *307*, 538−544.

(28) Mout, R.; Moyano, D. F.; Rana, S.; Rotello, V. M. Surface Functionalization of Nanoparticles for Nanomedicine. *Chem. Soc. Rev.* **2012**, *41*, 2539−2544.

(29) Zhang, C.; Li, C.; Huang, S.; Hou, Z.; Cheng, Z.; Yang, P.; Peng, C.; Lin, J. Self-Activated Luminescent and Mesoporous Strontium Hydroxyapatite Nanorods for Drug Delivery. *Biomaterials* **2010**, *31*, 3374−3383.

(30) Angelov, S.; Stoyanova, R.; Dafinova, R.; Kabasanov, K. Luminescence and EPR Studies on Strontium Carbonate Obtained by Thermal Decomposition of Strontium Oxalate. *J. Phys. Chem. Solids* **1986**, *47*, 409−412.

(31) Hu, L.-D.; Liu, Y.; Tang, X.; Zhang, Q. Preparation and in Vitro/in Vivo Evaluation of Sustained-Release Metformin Hydrochloride Pellets. *Eur. J. Pharm. Biopharm.* **2006**, *64*, 185−192.

(32) Wu, Y.-J.; Tseng, Y.-H.; Chan, J. C. C. Morphology Control of Fluorapatite Crystallites by Citrate Ions. *Cryst. Growth Des.* **2010**, *10*, 4240−4242.

(33) Gao, D.; Zhang, X.; Gao, W. Formation of Bundle-Shaped β-$NaYF_4$ Upconversion Microtubes via Ostwald Ripening. *ACS Appl. Mater. Interfaces* **2013**, *5*, 9732−9739.

(34) Zhao, Q.; Shao, B.; Lu, W.; Jia, Y.; Lv, W.; Jiao, M.; You, H. Tysonite Type $Gd_{1-y}Ca_yF_{3-y}$ Solid Solution: Hydrothermal Synthesis and Luminescence Properties. *CrystEngComm* **2013**, *15*, 9930−9937.

(35) Pifferi, A.; Taroni, P.; Torricelli, A.; Valentini, G.; Mutti, P.; Ghislotti, G.; Zanghieri, L. Nanosecond Time-Resolved Emission Spectroscopy from Silicon Implanted and Annealed SiO_2 Layers. *Appl. Phys. Lett.* **1997**, *70*, 348−350.

(36) Zhang, C.; Cheng, Z.; Yang, P.; Xu, Z.; Peng, C.; Li, G.; Lin, J. Architectures of Strontium Hydroxyapatite Microspheres: Solvothermal Synthesis and Luminescence Properties. *Langmuir* **2009**, *25*, 13591−13598.

(37) Voorhees, P. W. The Theory of Ostwald Ripening. *J. Stat. Phys.* **1985**, *38*, 231−252.

(38) Li, X.; Hanagata, N.; Wang, X.; Yamaguchi, M.; Yi, W.; Bando, Y.; Golberg, D. Multimodal Luminescent-Magnetic Boron Nitride

Nanotubes@$NaGdF_4$:Eu Structures for Cancer Therapy. *Chem. Commun.* **2014**, *50*, 4371−4374.
(39) Chen, Y.; Chen, H.; Zhang, S.; Chen, F.; Zhang, L.; Zhang, J.; Zhu, M.; Wu, H.; Guo, L.; Feng, J.; Shi, J. Multifunctional Mesoporous Nanoellipsoids for Biological Bimodal Imaging and Magnetically Targeted Delivery of Anticancer Drugs. *Adv. Funct. Mater.* **2011**, *21*, 270−278.
(40) Li, F.; Li, C.; Liu, X.; Chen, Y.; Bai, T.; Wang, L.; Shi, Z.; Feng, S. Hydrophilic, Upconverting, Multicolor, Lanthanide-Doped $NaGdF_4$ Nanocrystals as Potential Multifunctional Bioprobes. *Chem.—Eur. J.* **2012**, *18*, 11641−11646.
(41) Liu, Z.; Yi, G.; Zhang, H.; Ding, J.; Zhang, Y.; Xue, J. Monodisperse Silica Nanoparticles Encapsulating Upconversion Fluorescent and Superparamagnetic Nanocrystals. *Chem. Commun.* **2008**, 694−696.
(42) Ren, G.; Zeng, S.; Hao, J. Tunable Multicolor Upconversion Emissions and Paramagnetic Property of Monodispersed Bifunctional Lanthanide-Doped $NaGdF_4$ Nanorods. *J. Phys. Chem. C* **2011**, *115*, 20141−20147.
(43) Zeng, S.; Tsang, M.-K.; Chan, C.-F.; Wong, K.-L.; Fei, B.; Hao, J. Dual-modal Fluorescent/Magnetic Bioprobes Based on Small Sized Upconversion Nanoparticles of Amine-Functionalized $BaGdF_5$:Yb/Er. *Nanoscale* **2012**, *4*, 5118−5124.